Geometric shadowing from rippled $SrRuO_3/SrTiO_3$ surface templates induces self-organization of epitaxial $SrZrO_3$ nanowires

Jiaqing He,[1,*] Regina Dittmann,[1] Silvia Karthäuser,[1] and Enrique Vasco[2,†]
[1]*Institut für Festkörperforschung, Forschungzentrum Jülich GmbH, D-52425 Jülich, Germany*
[2]*Instituto de Ciencia de Materiales de Madrid, Consejo Superior de Investigaciones Científicas, 28049 Cantoblanco, Madrid, Spain*
(Received 28 July 2006; published 7 November 2006)

Structure, morphology, and conductivity of $SrZrO_3$ nanowires self-organized on rippled $SrRuO_3/SrTiO_3$ surface templates by pulsed laser deposition are investigated by transmission electron microscopy and atomic force microscopy using dc-poled conductive tips. The responsible mechanism for the self-organized growth of fully-relaxed epitaxial $SrZrO_3$ on the $SrRuO_3$ ripple tops is identified as geometric shadowing induced by both the surface template morphology and the broadening of the angular distribution of the flux of incident particles. The latter process reflects the interactions between the deposition gaseous atmosphere (here molecular oxygen is at pressures $\approx 10^{-1}$ mbar) and the ejected plume of laser-ablated particles. The broadening, as estimated from the average scattering angle of the particles within incident flux measured in an artificial shadowing experiment, served as input to simulate numerically the morphological evolution of the resulting nanostructured system, wired $SrZrO_3$/rippled $SrRuO_3/SrTiO_3$.

DOI: 10.1103/PhysRevB.74.205410 PACS number(s): 68.55.−a, 81.07.−b, 68.47.Gh, 68.37.Lp

I. INTRODUCTION

During the last few years, a great deal of effort in the scientific community has gone to nanostructuring inorganic systems. Top-bottom and bottom-up (the latter termed self-organization) approaches have been extensively and successfully explored.[1–4] In this context, metals and semiconductors[5,6] collect most of the spent efforts whereas the oxides—despite their promising functional properties receive minor attention. Within the oxides, those with perovskite structure are especially attractive due to their dielectric, electromechanical, and multiferroic properties that are suitable for high-performance applications given their chemical, thermal, and mechanical stability. Currently, preparation at laboratory scale of reliable nanoscale devices (e.g., arrays of nanometric multiferroic elements to be used as ultrahigh-density memory-store medium)[7] based on perovskite oxides is in progress. Within this framework, several self-organization routes have been investigated, some of the most common ones being:[8] (i) self-organization driven by interfacial stress originated during heteroepitaxial growths,[9,10] (ii) ordered segregations of immiscible chemical phases,[7,11] (iii) using surfaces with nanometric periodicities (e.g., vicinal surfaces),[12] (iv) via chemical routes based on hydrothermal deposition[13] and/or self-assembly lithography,[14,15] and (v) through three-dimensional (3D) thickness instabilities for ultrathin films (known also as self-patterning) due to the formation of thermally unstable unfavored interfaces.[16,17]

In an earlier work, we demonstrated the successful fabrication of Cr-doped $SrZrO_3$ (SZO) nanowires on rippled $SrRuO_3$ (SRO) templates $SrZrO_3$, which are prepared in situ on phototreated vicinal $SrTiO_3$ (STO) substrates.[18] The heterostructure of stacked oxides studied there was chosen attending to the following functional properties: Undoped SZO suits to high voltage capacitive applications due to its high dielectric constant ($\varepsilon \approx 60$) and breakdown strength (400 kV cm^{-1}),[19] while SZO doped with transition metals (e.g., Cr) is a promising candidate for resistance-switching nonvolatile memories.[20] Thus, Cr-doped SZO self-organized in nanometric one-dimensional (1D) or zero-dimensional (0D) elements would assist in scaling up memory densities towards the region of Gbits. SRO is used as bottom electrode due to its metallic conductivity at room temperature and its relatively good lattice match (mismatch $\approx$−0.6%) with STO(100). Its rippled morphology provides a template (as discussed below) for SZO self-organization and is consistent with a crossbar-device topology. STO is a popular substrate for the epitaxial growth of perovskites. The lattice-matched combination (100)SRO/(100)STO rules out any influence of stresses originated in the bottom-electrode/substrate interface on the growth mode of SZO.

In this work, we analyze thoroughly the influence of geometric shadowing, as phenomenon that is inherent in growths from vapor phase using pseudopointing evaporation sources, on the formation of SZO nanowires on rippled SRO templates. We will demonstrate that geometric shadowing plays a key role on this phenomenon and can consequently be regarded as an effective nanoengineering tool to promote the self-organization (and then the nanostructuration) of perovskite oxides on surface templates.

II. EXPERIMENTAL

Previous to the SZO growth, the rippled SRO template was prepared by pulsed laser deposition on phototreated STO(100). Its surface (as revealed by x-ray photoelectron spectroscopy, not shown here) is formed of TiO_2 finished terraces, which are separated from each other by one-unit-cell height SrO_2 enriched steps.[18] SRO epitaxially grows on several oxide substrates showing different growth modes depending on the system's lattice mismatch. Thus, SRO grows by step flow on as-received vicinal STO surfaces[21,22] (low mismatch $\approx$−0.6%) and by Stranski-Krastanov mode on singular $LaAlO_3$ surfaces (high mismatch $\approx$−3.5%), the latter giving rise to regularly rippled films.[10] SRO grows on phototreated STO surfaces with a two-dimensional (2D)-featured

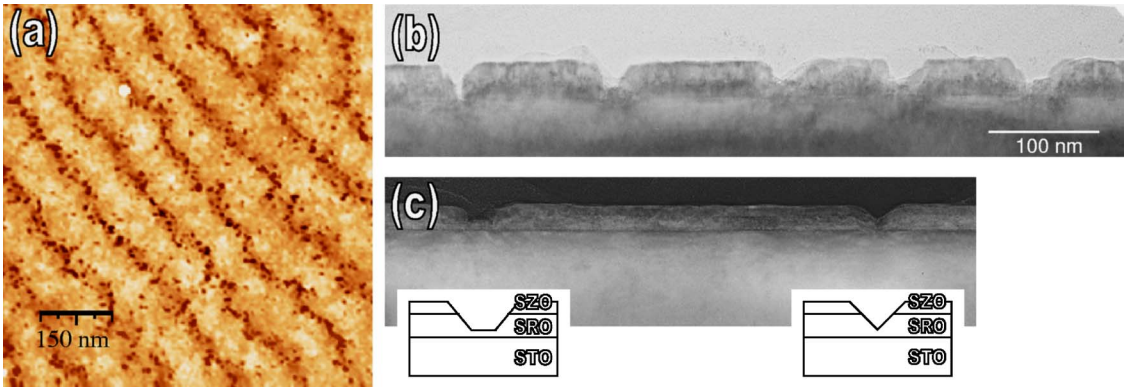

FIG. 1. (Color online) Surface morphology (a) and cross-sectional structure (b and c) imaged by AFM and TEM, respectively, of the heterostructure wired SZO/rippled SRO/STO. *Schemes in (c)*: Layered structures of two inter-ripple grooves with trapezoidal (*left*) and triangular shapes (*right*).

habit (i.e., initially layer-by-layer and step-flow later) except that the coalescence of elements nucleated on neighboring terraces is blocked by residual SrO_2 trapped in the steps.[18] This gives rises to a 3D-featured growth of SRO ripples confined laterally by STO steps. On the steps, the growth of SRO is partially inhibited, so that the resulting SRO film is considerably thinner than elsewhere. For this study, 10 nm thick SRO deposits were prepared.

SZO films were growth *in situ* (using a multitarget system) on thus-prepared rippled SRO/STO substrates by pulsed laser deposition. For that, a KrF excimer laser ($\lambda=248$ nm) emitting 16 ns pulses with an energy density of $J=5$ J cm^{-2} at a frequency of 10 Hz was focused on a SZO ceramic target, which was continuously rotated at 20 Hz. The substrates were distanced 60 mm opposite to the target and heated within the range of $T_s=650-800$ °C. The SZO films were grown in a high vacuum chamber (base pressure: 1×10^{-5} mbar) with an oxygen dynamic pressure of $PO_2=0.5$ mbar (except during the shadowing experiments in which PO_2 was as low as 10^{-4} mbar). Their average growth rate was about 1.8 ± 0.3 Å/s. We did not expect any changes in the morphology of the rippled SRO/STO substrate during the growth of SZO since the deposition conditions were similar to those previously used to deposit SRO on phototreated STO.

The epitaxial SZO films exhibit two out-of-the-plane orientations[23] (namely SZO[110]‖STO[001] and SZO[001]‖STO[001]), each formed of two in-plane alignments in a similar way to those of SRO epitaxed on STO despite the high lattice mismatch at the interface SZO/SRO ($\approx-4.4\%$). The combination of the different SRO and SZO orientations engenders between four and sixteen domains coexisting in the bulk of the heterostructure SZO/SRO/STO.[23]

Morphology and sample conductivity were simultaneously investigated by atomic force microscopy (AFM) in contact mode using a JEOL JSPM-4210A setup. Images were acquired with Pt/Ir coated silicon tips, which were +0.2 V dc poled with respect to the grounded sample.

The sample structure was investigated by transmission electron microscopy (TEM) using a JEOL 4000EX microscope. Cross-sectional specimens were imaged by high-resolution TEM (HRTEM). These specimens were prepared by cutting the SZO/SRO-covered STO wafer into slices, gluing together pairs of slices face to face, and embedded them in epoxy resin. Subsequently, the glue was cured and 3 mm diameter disks obtained by cutting away the excess epoxy. These disks were ground, dimpled, polished, and then Ar^+-ion milled on a stage cooled with liquid nitrogen.

For our experiments on geometric shadowing, a special sample holder with a noncontact fixed mask, which is separated 500 μm over the sample surface was employed. The width of the thickness gradient between shadowed and nonshadowed areas on the sample surfaces were measured by profilometry using a Sloan Dektak 3030 profilometer set-up equipped with an optical microscope whose output was coupled to an image processing system.

III. RESULTS

Surface morphology (as imaged by AFM) and cross-sectional structure (by low magnification TEM) of the SZO/SRO/STO heterostructure are shown in Figs. 1(a) and 1(b), respectively. The contrast analysis in Fig. 1(c) reveals that SZO grows preferentially on the tops of the SRO ripples, i.e., as isolated 1D islands (nanowires) such that the rippled SRO/STO morphology is preserved and the inter-ripple grooves became moderately deeper than initially before SZO growth, but not narrower. Figure 1 sketched two configurations of trapezoidal- and triangular-shaped grooves (left and right, respectively) whose aperture angles (ϕ) remain as quasiconstants. Different groove configurations are related to the local morphology of the SRO steps; thus triangular grooves are formed at straight line sections of the steps, whereas the trapezoidal ones originated in meandering sections with a high density of SrO_2 enriched kinks.

The SZO growth mode (i.e., forming wires on the tops of SRO ripples) was confirmed by mapping of the local electrical conductivity of the SZO/SRO/STO heterostructure. The conductivity map of rippled SRO/STO substrate (not shown) exhibits high conductivity with currents of 10 and 0.5 nA measured along and across the ripple axes, respectively. Once SZO grown [Fig. 2(a)], conductivity at the tops of the ripple (i.e., along their axes) drops by three orders of magnitude down to 0.01 nA, whereas conductivity at the grooves

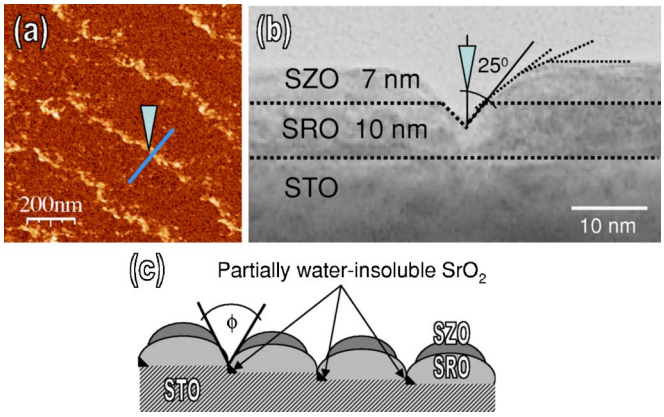

FIG. 2. (Color online) (a) +0.2 V dc-conductivity mapping of the wired SZO/rippled SRO surface. (b) Details of an inter-ripple groove nearby region imaged by TEM. Interfaces between layers are denoted by dotted thick lines. (c) Outline of the SZO/SRO/STO heterostructure topology.

remains unchanged. This result allows us to ascribe the dark areas and the light ones to insulating SZO nanowires and uncovered SRO grooves, respectively. Figure 2(b) shows at higher magnification details of a nearby-groove region whose multilayered structure is clear. The interfaces between the labeled layers are denoted by dotted lines. It is apparent that the SZO wires are unconnected across the grooves. The inner aperture angle of the grooves [as shown in Fig. 2(b)] is estimated to be $\phi=50\pm10°$ (note the image aspect ratio from the calibrated layer thicknesses and the lateral scale). This angle increases as it approaches the surface (see progression of dotted lines at the groove's right wall), and then the grooves emerge smoothly on the surface, such that the ripples exhibit rounded edges. A sketch summarizing the SZO/SRO/STO heterostructure topology according to above results is depicted in Fig. 2(c).

Cross-sectional HRTEM images corresponding to the bulk region of a ripple are displayed in Figs. 3(a) (zone axis∥STO[100]), 3(b) (∥STO[100]) and 3(c) (∥STO[110]). Horizontal arrows point to the interfaces between layers, whereas the misfit dislocations and other kinds of defects are marked, respectively, by vertical and oblique arrows. The high lattice mismatch between SZO and SRO ($\approx-4.4\%$) can be accommodated either by remaining strain or via the formation of misfit dislocations at the interface between them depending on their elastic properties and thicknesses. Figure 3(a) shows a periodic network of misfit dislocations at the SZO/SRO interface (as indicated by oblique arrows). The spacing between dislocations averaged over large lengths (in $\approx$100-nm width terraces) along the interface is 12 ± 2 nm. This spacing, which is larger that that expected for a fully relaxed film ($\approx$9 nm),[18] suggests that SZO film remains $-1\pm0.5\%$ strained. Burgers circuits around the dislocation cores in Fig. 3(b) yield a closure failure with a perfect vector $a[100]$, a being the pseudocubic perovskite lattice used to describe the SZO orthorhombic structure. Some misfit dislocations with Burgers vector $a/2[1\bar{1}0]$ are pointed out [Fig. 3(c)] at both SZO/SRO and SRO/STO interfaces. Since this vector does not correspond to a lattice translation and no

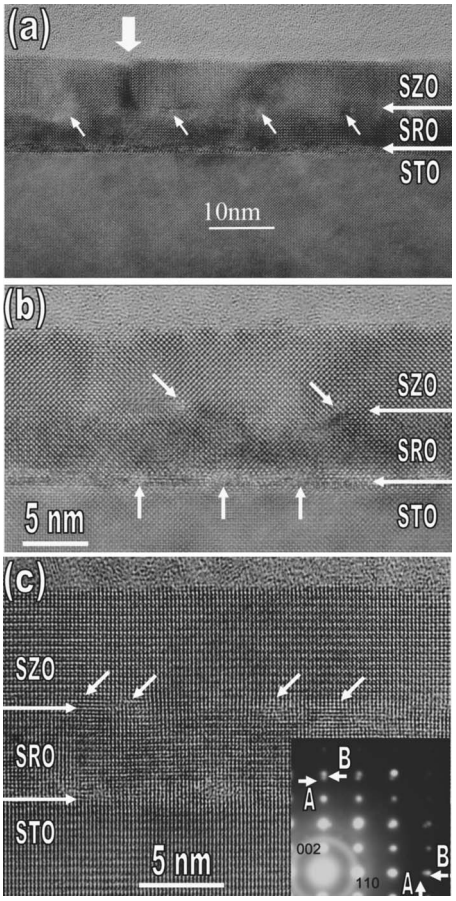

FIG. 3. Series of HRTEM images (sorted from the top by increasing magnification) of the bulk region of a ripple. Vertical and oblique arrows point to defects and misfit dislocations, whereas horizontal ones indicate the interfaces between layers. The zone axes are STO[100] (a and b) and STO[110] (c). *Inset in (c)*: Selected-area electron diffraction pattern acquired along STO[110].

other related defects are found within the nearby area, its magnitude can be correlated with the (110)-projected components of the Burgers vector for a perfect dislocation. Thus, from Figs. 3(b) and 3(c), the displacement vector $a/2[1\bar{1}0]$ can be unambiguously identified as an in-(110) plane component of an $a[100]$ dislocation. Planar defects [as that denoted by the white thick down-arrow in Fig. 3(a)] are rarely detected within the SZO film bulk, suggesting imperfect coalescence of SZO islands nucleated on the same terrace.

The inset in Fig. 3(c) displays a selected-area electron diffraction pattern acquired along STO[110] zone axis using an aperture that simultaneously collects diffractions coming from the SZO film, the SRO bottom layer, and STO substrate. Two split diffracted spots indexed as 008 and 330, respectively ascribed to SZO (labeled A) and SRO/STO (B), are perceptible along both the out-of-the-plane and in-plane directions. From an accurate image calibration employing digital micrograph processing software and the cubic STO lattice parameter ($a_{STO}=0.3905$ nm) as a calibration standard, we determine both the in-plane $a_{\parallel}=0.4083$ nm and out-of-the-plane $a_{\perp}=0.4089$ nm SZO lattice parameters, which indicate that the SZO film is mostly relaxed. This result dis-

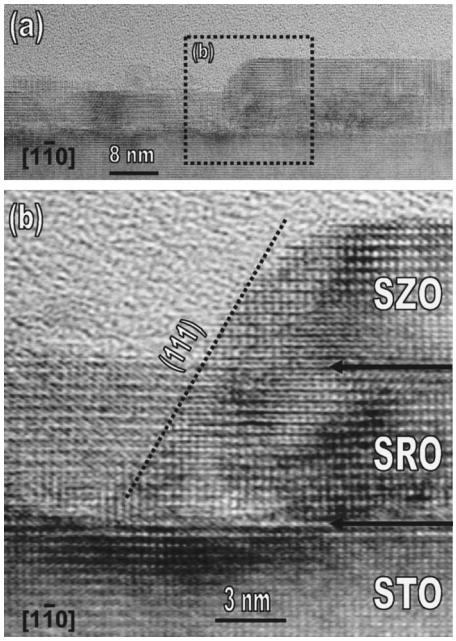

FIG. 4. TEM and HRTEM images (a and b, respectively) of the inter-ripple groove nearby region of a ripple at a wired SZO/rippled SRO/STO heterostructure. Horizontal arrows indicate the interfaces between layers. The zone axis for both images is STO[110].

agrees with our previous estimate of a −1% level of compressive strain remaining in the SZO film, which was deduced from the average spacing between dislocations. A plausible explanation for this discrepancy evokes the existence of a complementary strain-relaxation mechanism (e.g., the detected planar defects), which could release the fraction of the mismatch strain not relaxed by the misfit dislocation network.

Figure 4 shows cross-sectional HRTEM images collected along STO[110] of a groove nearby area. The magnified lattice image [Fig. 4(b)] reveals that a large fraction of the groove's walls is (111) faceted. Facets with higher tilts with respect to substrate plane at the groove's narrowest region could not be discerned because of difficulties in accurately resolving these regions due to the presence of substrate-parallel antiphase boundaries (APBs). The overlapping visual effect of the imaged lattices in these regions is a consequence of the APB planes not lying parallel to the zone axis. APBs also might operate as a complementary strain-relaxation mechanism.

The preferential growth of the SZO films on the tops of the SRO ripples, contrary to the system's thermodynamic tendency towards states of minimum energy induced by surface curvature-driven diffusions (i.e., the groove filling), points to a growth kinetics ruled by a mechanism of the geometric shadowing of the grooves (the most depressed surface features) by the neighboring ripples (prominent features). This mechanism would imply a non-null angular distribution (for angles departing from the perpendicular one to the surface) of the flux of the particles evaporated on the growing surface. To investigate the angular dependence of such a flux [$\Omega(\theta)$, generated here by PLD], the following experiment was performed: A portion of the substrate surface (here bare STO) was artificially shadowed by a mask [the geometry is depicted in Fig. 5(a)]. The optic contrast due to a thus-prepared thickness gradient in a $PO_2 = 5 \times 10^{-1}$ mbar film is displayed in Fig. 5(b). The contrast within the enclosed region (that at the bottom of the image) has been enhanced by plotting the derivative as colored contour curves in the inset of Fig. 5(b). The average widths of the thickness gradients (x) produced by the mask edge (color gradient [rainbow online] region delimited in Fig. 5(b)) in 1 μm thick SZO films deposited at oxygen pressures of 10^{-4} and 5×10^{-1} mbar were determined by profilometry and tested by optical image processing to be $x = 80 \pm 20$ and 440 ± 50 μm, respectively. The average scattering angle $\langle \delta\theta \rangle$ of the incident flux [approximately full width at half maximum, fwhm, of $\Omega(\theta)$], which is measured from the substrate normal, is directly estimated from the width of the thickness gradient and the sample-mask separation (here $y \approx 500$ μm) as: $\tan(\langle \delta\theta \rangle / 2) = x/2y$. It results in $\langle \delta\theta \rangle \approx 9 \pm 1$ and $\langle \delta\theta \rangle \approx 48 \pm 1°$ for oxygen pressures of 10^{-4} and 5×10^{-1} mbar, respectively.

The angular dependence of the flux for nonthermal evaporations from a pointing source (e.g., an ablation spot) on a semi-infinite plane (e.g., target surface) was fit to a forward peak-type relationship:[24] $\Omega(\theta) \propto \cos^{\nu+3}(\theta)$ with $\nu+3$ describ-

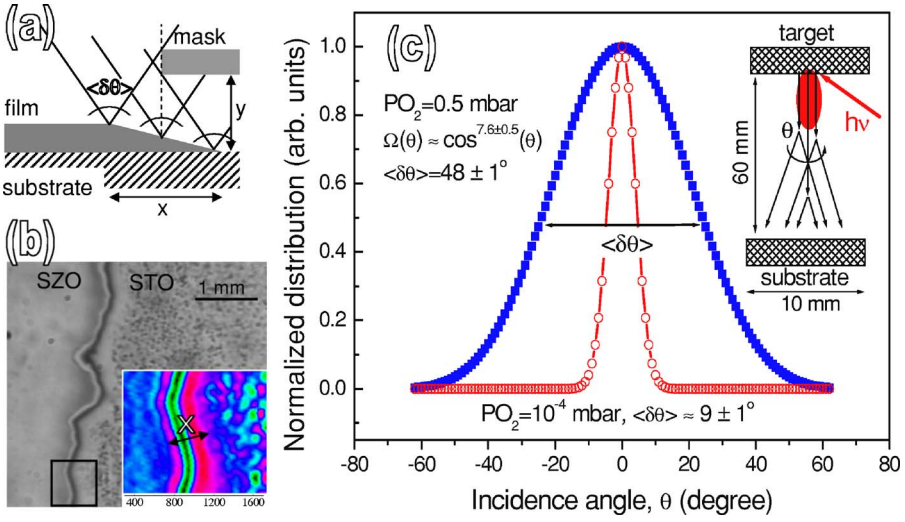

FIG. 5. (Color online) Geometry (a and *sketch in c*) and results (b and c) of the designed artificial shadow experiment. (a) Geometric considerations concerning the shadow generated by a mask. (b) Optic contrast (raw and derivative, the latter in the contour plot inset) due to the gradient of thickness between the uncovered substrate area and the shadowed one. (c) Generated curves of angular distribution of arriving particles per incidence angle for different deposition oxygen pressures (open circle, $PO_2 = 10^{-4}$ mbar solid square, $PO_2 = 0.5$ mbar).

ing the degree of collimation of the semispherical flux emitted per solid angle directed to a planar substrate. Here, $\nu = 1$ corresponds to an uncollimated thermal evaporation, such as those used in standard chemical vapor depositions. The normalized $\Omega(\theta)$ curves shown in Fig. 5(c) for different oxygen pressures ($PO_2 = 10^{-4}$ mbar, open circles; and 0.5 mbar, solid squares) were simulated from their estimated $\langle \delta\theta \rangle$ values according to the fwhm-condition:[24] $\Omega(\langle \delta\theta \rangle/2) = 1/2$. The spherical symmetry of the process (since the pseudopointing shape of the ablation spot) determines a threshold uncertainty of $\approx 9°$ (10 mm of substrate size per 60 mm of substrate-target separation) for the angle of incidence, and thus, smaller $\langle \delta\theta \rangle$ cannot be discerned reliably. $\langle \delta\theta \rangle$ is around the threshold uncertainty for SZO films grown at $PO_2 = 10^{-4}$ mbar, whereas $\langle \delta\theta \rangle \approx 48 \pm 1°$ (which corresponds to $\nu = 4.66 \pm 0.5$) for those deposited at higher pressures ($PO_2 = 5 \times 10^{-1}$ mbar). It should be stressed that the average scattering angle of the incident flux $\langle \delta\theta \rangle \approx 48 \pm 1°$ estimated for standard deposition conditions (as those used here: where $PO_2 \geqslant 10^{-1}$ mbar to avoid oxygen nonstoichiometry that is of prime relevance for the functional properties of perovskite oxides) is plausibly close (i.e., within error bar) to the aperture angles of the inter-ripple grooves as measured from TEM images ($\phi = 50 \pm 10°$) in Fig. 2.

IV. DISCUSSION

The findings presented above pointing to: (i) a distinctive SZO growth mode characterized by the preferential growth of unconnected insulating nanowires on the tops of SRO ripples; and (ii) the existence of deepening grooves exhibiting quasi-constant aperture angles, which are close to the average scattering angle estimated for the incident flux under standard deposition conditions; demonstrate unambiguously the key role played by the geometric shadowing in this system. Thus, the geometric shadowing would act as surface destabilization mechanism counterbalancing the system's dynamics embodied by the downhill diffusion towards the grooves (stabilizing mechanism). Geometric shadowing requires a non-null distribution of impinging particles per incidence angle that is different from the perpendicular one; such that the number of particles arriving per time unit on a given surface site depends on its local aperture angle, which is determined *a priori* by the topology of the surface template (rippled SRO/STO). The equation describing the evolution of the surface morphology $h(\vec{r},t)$ from the surface template $h(\vec{r},0)$ is as follows:[25,26]

$$\frac{\partial h(\vec{r},t)}{\partial t} = \frac{F}{\psi}\int_{\phi_l(\vec{r},t)}^{\phi_r(\vec{r},t)} \Omega(\theta)\partial\theta - \kappa\nabla^4 h(\vec{r},t) + \eta(\vec{r},t), \quad (1)$$

where F is the θ-independent net flux; $\Omega(\theta)$ is the angular dependence of the flux estimated in Fig. 5; $\psi = \int_{-\pi/2}^{\pi/2}\Omega(\theta)\partial\theta$ is a normalization factor; ϕ_l (ϕ_r) corresponds to the left (right) aperture angle measured from the surface normal, such that $\phi(\vec{r},t) = \phi_l(\vec{r},t) + \phi_r(\vec{r},t)$; and κ is a diffusion-coefficient proportional constant. First term in Eq. (1) describes the local aperture-angle dependence of the geometric shadowing from the angular distribution of the flux of incident particles. The second one accounts for the surface-curvature driven diffusion (Mullins's diffusion),[27,28] while the third term corresponds to the Gaussian white noise related to random fluctuations in the deposition process. This latter term fulfills the following conditions for a growth in $d+1$ dimensions:[28] (i) $\langle \eta(\vec{r},t) \rangle = 0$; and (ii) $\langle \eta(\vec{r}_1,t_1)\eta(\vec{r}_2,t_2) \rangle = 2\eta_0\delta^d(\vec{r}_1 - \vec{r}_2)\delta(t_1 - t_2)$, i.e., it is uncorrelated in space and time, its amplitude being $\eta_0 \propto \sqrt{F}$.

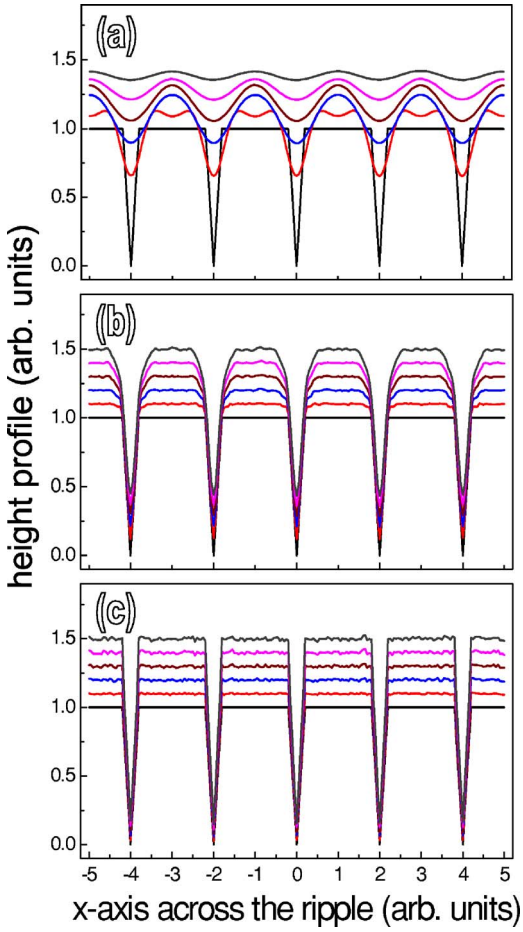

FIG. 6. (Color online) Numerical solutions of Eq. (1) for different κ/F ratios (a): $\kappa/F = 10^{-3} \ldots 10^{-2}$; b: 5×10^{-6}; and c: 10^{-8}). The fitting parameters are $F = 1$, $\psi = 0.88$, and 20% of the surface sample covered by grooves. The curve series for each κ/F ratio shows the morphology evolution for increasing runtimes (from bottom) of $t = 0$, 100, 200, 300, 400, and 500 time steps ($\Delta t = 10^{-3}$).

Equation (1) was integrated in 1D across the ripple axes (since the symmetry of the wired SZO/rippled SRO/STO samples) by the Runge-Kutta method assuming periodic boundary conditions. Its numerical solutions for different κ/F ratios, shown in Fig. 6, provide an estimation of the balance between geometric shadowing and surface diffusion. For a high κ/F ratio ranging between 10^{-3} and 10^{-2} [Fig. 6(a)], the system's nanostructuration tends to disappear by preferential groove filling that induces the ripples to coalesce rapidly. On the other hand, for κ/F ratios lower than 10^{-8} [i.e., diffusion-inhibited growth regimes, Fig. 6(c)], the grooves are deeper and narrower, the ripple's edges are

abrupt, and geometric shadowing becomes a self-sustained mechanism exerting an increasing influence on growth kinetics as the deposition proceeds. For intermediate κ/F ratios, as that shown in Fig. 6(b) where $\kappa/F=5\times10^{-6}$, grooves develop quasiconstant aperture angles and ripples with rounded edges. This latter simulated topology resembles to those imaged by TEM in our nanostructured SZO/SRO/STO samples. Thus, we conclude that our simulation closely reproduces the self-organization phenomenon resulting from geometric shadowing of oxides growing on surface templates.

In the system studied here, the self-organized growth is a direct consequence of both the surface template and the geometric shadowing induced by broadening of the angular distribution of the flux of incident particles; broadening that takes place as the oxygen pressure rises. The connection between $\Omega(\theta)$ and oxygen can be expressed in terms of the interaction of the ablation plume with the deposition atmosphere: Thus, during PLD a forward-peaking high-density sharp plume of ablated species is ejected. The background oxygen pressure influences on the ballistic trajectory of these species in two ways: (i) by multiple scattering with the oxygen molecules, and (ii) by spatial confining of the plume, thereby promoting inner collisions between the ablated species. The scattering of the species within the plume is inhomogeneous; the slight ones being more susceptible to be scattered. In particular, atomic Sr exhibits a large cross section of collision with oxygen so that a preferential scattering is foreseen for this species.[29] Due to the perovskite phase admits a reduced stoichiometry deviation upon its nucleation (i.e., basically, it nucleates in the stoichiometric phase),[30] the effectiveness of the self-organization induced by geometric shadowing is enhanced since it requires the preferential scattering of any of the involved species. Alternatively, the process effectiveness is also envisioned for simple (nonmulticationic) oxides where extensive phenomena of geometric shadowing have been detected, e.g., in PLD-grown ZnO.[31]

V. CONCLUSION

We successfully explored the mechanisms involved in the self-organized growth of SZO by geometric shadowing on rippled SRO/STO templates. This growth gives rise to an array of unconnected insulating nanowires, whose configuration is suitable for crossbar-topology devices. The structure, morphology, and conductivity of the self-organized nanowire SZO/rippled SRO/STO epitaxial heterostructures were investigated by (HR)TEM, AFM, and dc-conductive AFM, respectively. Finally, the key role played on the self-organization phenomenon by the mechanism of geometric shadowing was corroborated by numerical simulations that reproduce the heterostructure morphology from experimental data achieved from a designed artificial shadowing experiment.

ACKNOWLEDGMENT

E.V. acknowledges and appreciates the support from the Spanish Education and Science ministry under the Ramón y Cajal program.

*Present address: Center for Functional Nanomaterials, Bldg. 480, Brookhaven National Laboratory, Upton NY-11973, USA.
†Corresponding author. Electronic address: enrique.vasco@icmm.csic.es

[1] S. Mann and G. A. Ozin, Nature (London) **382**, 313 (1998).
[2] B. A. Korgel and D. Fitzmaurice, Phys. Rev. Lett. **80**, 3531 (1998).
[3] F. Liu, J. Tersoff, and M. G. Lagally, Phys. Rev. Lett. **80**, 1268 (1998).
[4] H. Omi, D. J. Bottomley, Y. Homma, and T. Ogino, Phys. Rev. B **67**, 115302 (2003).
[5] C. J. Kiely, J. Fink, M. Brust, D. Bethell, and D. J. Schiffrin, Nature (London) **396**, 444 (1998).
[6] R. Heitz, A. Kalburge, Q. Xie, M. Grundmann, P. Chen, A. Hoffmann, A. Madhukar, and D. Bimberg, Phys. Rev. B **57**, 9050 (1998).
[7] H. Zheng, J. Wang, S. E. Lofland, Z. Ma, L. Mohaddes-Ardabili, T. Zhao, L. Salamanca-Riba, S. R. Shinde, S. B. Ogale, F. Bai, D. Viehland, Y. Jia, D. G. Schlom, M. Wuttig, A. Roytburd, and R. Ramesh, Science **303**, 661 (2004).
[8] M. Alexe and D. Hesse, J. Mater. Sci. **41**, 1 (2006).
[9] J. C. Jiang, L. L. Henry, K. I. Gnanasekar, C. L Chen, and E. I. Meletis, Nano Lett. **4**, 741 (2004).
[10] E. Vasco, R. Dittmann, S. Karthauser, and R. Waser, Appl. Phys. Lett. **82**, 2497 (2003).
[11] M. Alexe, J. F. Scott, C. Curran, N. D. Zakharov, D. Hesse, and A. Pignolet, Appl. Phys. Lett. **73**, 1592 (1998).
[12] F. Sanchez, G. Herranz, J. Fontcuberta, M. V. Garcia-Cuenca, C. Ferrater, and M. Varela, Phys. Rev. B **73**, 073401 (2006).
[13] I. Szafraniak and M. Alexe, Ferroelectrics **291**, 19 (2003).
[14] M. E. Coda, H. H. Du, S. Bhandarkar, and D. W. Johnson, Supramol. Sci. **4**, 43 (1997).
[15] W. H. Ma, D. Hesse, and U. Gosele, Small **1**, 837 (2005).
[16] A. Roelofs, T. Schneller, K. Szot, and R. Waser, Nanotechnology **14**, 250 (2003).
[17] I. Szafraniak, C. Harnagea, R. Scholz, S. Bhattacharyya, D. Hesse, and M. Alexe, Appl. Phys. Lett. **83**, 2211 (2003).
[18] E. Vasco, S. Karthauser, R. Dittmann, J. Q. He, C. L. Jia, K. Szot, and R. Waser, Adv. Mater. (Weinheim, Ger.) **17**, 281 (2005).
[19] R. V. Shende, D. S. Krueger, G. A. Rossetti, and S. J. Lombardo, J. Am. Ceram. Soc. **84**, 1648 (2001).
[20] A. Beck, J. G. Bednorz, C. Gerber, C. Rossel, and D. Widmer, Appl. Phys. Lett. **77**, 139 (2000).
[21] J. C. Jiang, W. Tian, X. Q. Pan, Q. Gan, and C. B. Eom, Appl. Phys. Lett. **72**, 2963 (1998).
[22] J. Choi, C. B. Eom, G. Rijnders, H. Rogalla, and D. H. A. Blank, Appl. Phys. Lett. **79**, 1447 (2001).
[23] S. Karthauser, E. Vasco, R. Dittmann, and R. Waser, Nanotechnology **15**, S122 (2004).
[24] *Pulsed Laser Deposition of Thin Films*, edited by D. B. Chrisey

and G. K. Hubler (John Wiley and Sons, New York, 1994), Chap. 7.
[25] R. P. U. Karunasiri, R. Bruinsma, and J. Rudnick, Phys. Rev. Lett. **62**, 788 (1989).
[26] C. Roland and H. Guo, Phys. Rev. Lett. **66**, 2104 (1991).
[27] W. W. Mullins, J. Appl. Phys. **28**, 333 (1957).
[28] A.-L. Barabási and H. E. Stanley, *Fractal Concepts in Surface Growth* (Cambridge University Press, Cambridge, 1995).
[29] J. Gonzalo, C. N. Afonso, and J. Perriere, Appl. Phys. Lett. **67**, 1325 (1995).
[30] E. Vasco, O. Böhme, E. Román, and C. Zaldo, Appl. Phys. Lett. **78**, 2037 (1995).
[31] E. Vasco, C. Zaldo, and L. Vázquez, J. Phys.: Condens. Matter **13**, L663 (2001).